metals

MDPI

Article

The Influence of Precipitation Hardening on the Damping Capacity in Al–Si–Mg Cast Components at Different Strain Amplitudes

Vitor H. Carneiro [1,*], José Grilo [2], Delfim Soares [2], Isabel Duarte [3] and Hélder Puga [2]

[1] MEtRICs, Campus of Azurém, University of Minho, 4800-058 Guimarães, Portugal
[2] CMEMS-UMinho, Campus of Azurém, 4800-058 Guimarães, Portugal; jl.coelho.grilo@gmail.com (J.G.); dsoares@dem.uminho.pt (D.S.); puga@dem.uminho.pt (H.P.)
[3] Department of Mechanical Engineering, Centre for Mechanical Technology and Automation (TEMA), University of Aveiro, 3810-193 Aveiro, Portugal; isabel.duarte@ua.pt
* Correspondence: d6705@dem.uminho.pt

Abstract: An A356 alloy is a classic casting light alloy, which is able to be processed into complex geometrical shapes with tailored static and dynamic mechanical properties. As a promising material to reduce fuel and energy consumption in future vehicle designs, there is an interest in understanding the impact of heat treatments on the damping capacity of this alloy. The Granato–Lücke theory is used to detail the forced vibration response in gravity cast A356. It is shown that a solution treatment enhances damping capacity in lower stress states (i.e., strain-independent regime) due to the increase in weak pinning length. However, in high-stress states (i.e., strain-dependent regime), peak-aged (T6) samples display higher damping capacity. This is proposed to be originated by releasing dislocations from weak pinning points, which start bowing in the precipitates that act as strong pinning points. Based on these results, it is shown for the first time that the selection of heat treatments to optimize damping in forced vibration is highly dependent on the expected stress–strain state and must be considered in the design of cast components.

Keywords: damping capacity; A356; heat treatment; metal casting; dislocations

Citation: Carneiro, V.H.; Grilo, J.; Soares, D.; Duarte, I.; Puga, H. The Influence of Precipitation Hardening on the Damping Capacity in Al–Si–Mg Cast Components at Different Strain Amplitudes. *Metals* **2022**, *12*, 804. https://doi.org/10.3390/met12050804

Academic Editor: Nikki Stanford

Received: 13 April 2022
Accepted: 4 May 2022
Published: 6 May 2022

1. Introduction

Current environmental concerns require the design and manufacturing of lightweight vehicles with high specific mechanical properties, such as strength-to-weight ratio and damping capacity. While load-bearing capacity is essential to produce light mechanical components to reduce fuel and energy consumption, enhancing damping capacity decreases fatigue-related issues and addresses life cycle concerns.

The A356 is a classic hypoeutectic casting aluminum alloy, being extensively used in the automotive, railway and aeronautic industries. Given its ability to be heat treated [1], it may have its static and dynamic mechanical properties tailored to be optimized to specific applications [2]. Additionally, it is characterized by good castability [3], resistance to corrosion [4] and its ability to be processed into thin-walled and complex geometries [5,6].

While numerous researchers have focused on the impact of light-alloy processing on yield and ultimate tensile strengths [7], there is recent concern about their damping capacity. These are frequently concerned with correlating microstructural changes to dissipate energy due to internal friction.

Y. Zhang et al. [8,9] showed that α-Al refinement in A356 alloys enhances the damping capacity at low strain amplitudes. M.N. Mazlee et al. [10] showed that the combination of α-Al and eutectic Si refinement by superheating an A357 alloy increases grain boundary damping. J.I. Rojas et al. [11] analyzed the damping increase in A356 by adding ceramic-based reinforcements, detailing the changes in thermoelastic relaxation peaks. Recently,

we also showed that a solution heat treatment enhances free-vibration damping capacity, while the dislocation pinning promoted in artificial aging reduces this property [2,12]. The interaction between the elastic modulus and damping capacity in post-solutionized and early artificial aging states also seems to be beneficial in reducing resonant stress in cast components and contributes to extending their life [13].

Dynamic loading is frequently characterized as forced vibration, meaning that the imposed strain is considered a variable [14]. Considering that Granato and Lücke [15] have long shown that forced vibration response is significantly dependent on strain amplitude, it is important to analyze the damping capacity of light alloys in this regime. This study reports the changes in the damping of A356 alloys as the strain is increased and considers different heat treatment stages. Experimental results show that the enhanced damping capacity may be achieved by selecting a solution treatment or artificial aging in the design phase, depending on the expected stress–strain states.

2. Materials and Methods

2.1. Melt Processing and Casting

An A356 alloy primary fusion ingot (composition in Table 1) was sectioned in 1kg lots, being afterward degreased, cleaned and dried to prevent melt contamination. Two 1 kg lots (i.e., 2 kg in total) were inserted in a Silicon Carbide (SiC) crucible placed within a resistance furnace. Both crucible and furnace were previously pre-heated to 680 ± 5 °C (5 h) to remove moisture and melt contamination with hydrogen.

Table 1. A356 chemical composition.

Element	Si	Mg	Fe	Ti	Cu	Mn	Zn	Res.	Al
% wt	7.44	0.30	0.13	0.11	0.07	0.07	0.05	0.12	Bal.

When melting was observed, a type-K thermocouple was inserted in the melt to measure the temperature and after it reached 720 °C it was allowed to homogenize for 15 min. After the homogenization period, the pre-heated SiAlON sonotrode (diameter, 60 mm) was inserted in the melt and ultrasonic vibration (600 W electric power, 20.2 ± 0.4 kHz) was applied for 2 min for degassing and refinement purposes. The melt was then poured into a steel die (pre-heated—250 °C) to produce 4 cylindrical samples (diameter and length, respectively, 14 mm and 150 mm).

Cylindrical samples were subjected to a T6 heat treatment by initially performing a solution treatment (T4) at 540 °C for 8 h followed by a quench in mild water. The solutionized samples were then artificially aged at 160 °C for 6 h and were then quenched in mild water. Samples were kept and cooled for storage in their as-cast, solution-treated (T4) and artificially aged (T6) state.

2.2. Microstructural Characterization

The cylindrical cast samples were sectioned to analyze the microstructure. These samples were initially ground with SiC papers down to 11 granulometry and, finally, polished with a 1 µm diamond solution. An optical microscope (Leica DM2500M) was used to observe the size and aspect ratio of the α-Al and eutectic Si. Data for this characterization were collected according to ASTM E112 in 50 measurements per optical field (100×) in 5 different fields, while the secondary dendrite arm spacing (SDAS) was determined as reported by interception method reported by E. Vanderluis and C. Ravind [16]. The microstructures of the samples were detailed by scanning electron microscopy with energy dispersive spectroscopy (SEM-EDS, Hitachi SU-70 with Bruker QUANTAX 400).

Hardness testing (Vickers) was carried out by Shimadzu HMV-2 equipment, by marking indentations on polished samples with a diamond square-based pyramid with a 0.1 Kgf load (15 s). These average hardness values and standard deviation were deter-

mined by 10 indentations in 5 samples for testing conditions (i.e., as-cast, solution-treated and peak-aged).

Thermal analysis was used to analyze the samples' melting temperature profiles and energies. Differential thermal analysis (DTA, TA instruments SDT 2960) was used to monitor the melting of the eutectic and secondary phases by performing a temperature ramp to 700 °C in the as-cast samples. Differential scanning calorimetry (DSC, TA instruments Q20) was also used to monitor precipitate melting in the solution-treated (T4) and artificially aged (T6) samples, by performing a temperature ramp to 400 °C. DTA and DSC routines were executed using a 10 °C/min heating rate with inert (Argon) atmosphere.

2.3. Dynamic Mechanical Analysis (DMA)

Rectangular specimens were extracted from the as-cast samples before being heat treated. These specimens were cut with a diamond disk and coolant to prevent precipitation due to local heating, with 35 × 5 × 2 mm^3 dimensions (0.1 mm tolerance). Specimens were subjected to the T4/T6 heat treatments and clamped to the equipment in a cantilever configuration to test their isothermal (room temperature, 25 °C) damping capacity over a wide range of strain amplitudes (1×10^{-3} to 3×10^{-2}) at 1 Hz. Prior to testing, heat-treated samples in their as-quenched state were immediately placed in a freezer to prevent precipitation.

3. Results and Discussion

Microstructural Analysis

Figure 1 displays the microstructures of the cast samples, in which the shape/tmorphology and size of the α-Al and eutectic Si may be analyzed. The lower magnifications (10×) in Figure 1 show the shape of the α-Al, respectively, in the as-cast (Figure 1a) and solution-treated (Figure 1c) samples. It may be observed that they are characterized by the globular and rosette morphologies in both cases. As expected, there is no significant difference between both samples, as solution-treated samples derive from the original as-cast state, which should not significantly modify the morphology of the α-Al.

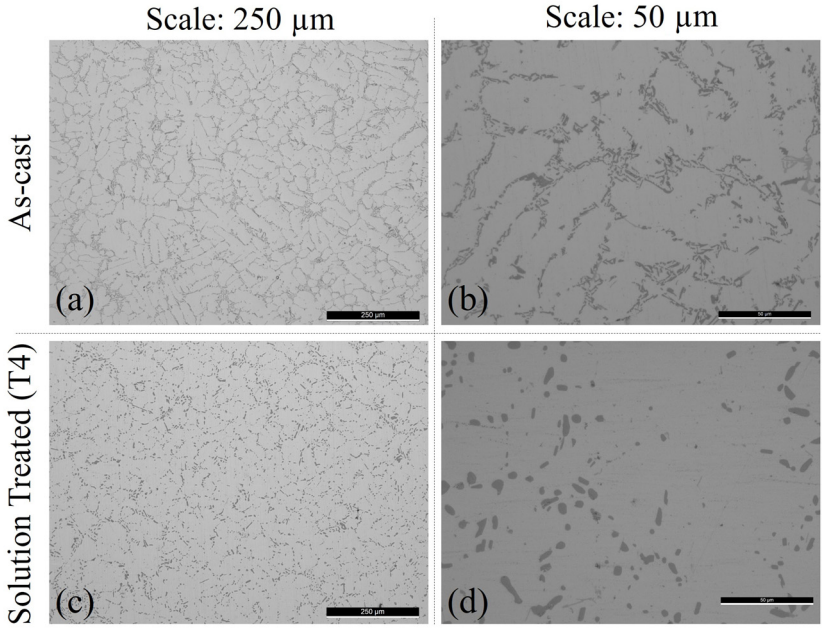

Figure 1. Optical microscopies detailing microstructures: (**a**,**c**) as-cast and (**b**,**d**) solution-treated (T4).

Grain refinement is more efficient near *liquidus* temperature [17,18], due to the reduction in nuclei survival time at high temperatures [19]. Given the lower melt viscosity and higher hydrogen diffusion at higher temperatures [20], the melt was successfully degassed

by the ultrasonic melt treatment, as no porosity may be found (Figure 1b). As presented in Table 2, it was determined that the solution-treated (T4) samples had a slight increase in SDAS due to accommodation of the solutionized eutectic Si [2].

Table 2. Geometrical characterization of α-Al and eutectic Si.

Microstructural Characterization		As-Cast	Solution-Treated (T4)
α-Al	SDAS (μm)	38 ± 14	39 ± 14
Eutectic Si	Area (μm^2)	4.7 ± 2.9	13.9 ± 4.6
	Aspect ratio (-)	3.0 ± 1.6	1.7 ± 0.7

Figure 1 and Table 2 also show that the solution treatment changed the eutectic Si area and aspect ratio. The increase in eutectic Si area (4.7 ± 2.9 to 13.9 ± 4.6) implies Si agglomeration due to Si self-diffusion and Si–Al interdiffusion [21]. The decrease in the aspect ratio (3.0 ± 1.6 to 1.7 ± 0.7) of the eutectic Si proves that the solution treatment thermally activated the Si and promoted spheroidization [22,23]. Both Si agglomeration and spheroidization are evidence of the successful solution treatment (Figure 1d), highlighted in the SEM micrograph and EDS mapping in Figure 2. Given that α-Al and eutectic Si are not significantly changed during artificial aging [2], peak-aged (i.e., T6) samples were not characterized by optical microscopy. Figure 2d–f also show that Fe-rich intermetallic compounds were also observed in the forms of thin-needles β-phases (β-AlFeSi) and polyhedral α-AlSiMgFe, as is usual in Al–Si–Mg alloys with ultrasonically treated melts.

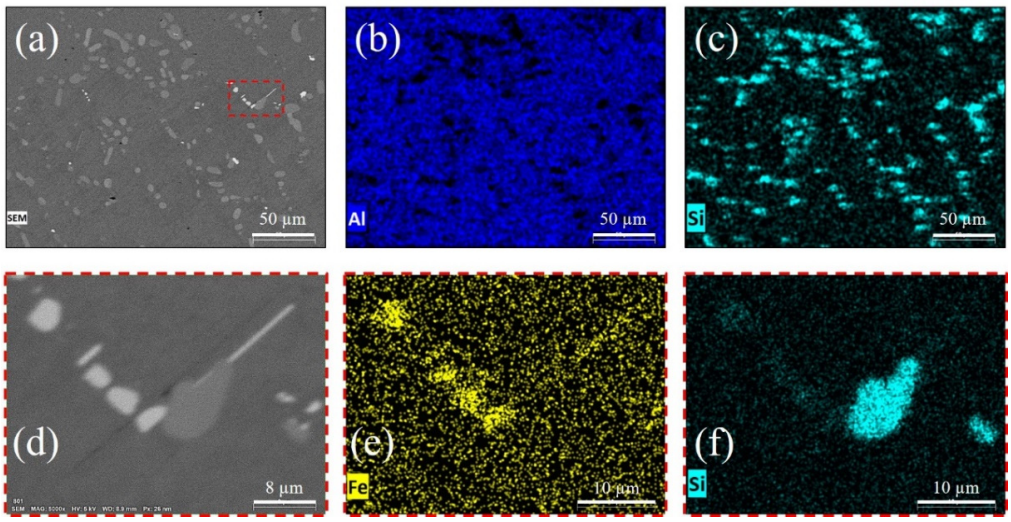

Figure 2. Detail of solution-treated (T4) sample with (**a**) micrograph and EDS mapping on (**b**) Al matrix and (**c**) eutectic Si; Higher magnification (**d**) micrograph with EDS mapping to detail (**e**) Fe-rich intermetallic compounds and (**f**) spheroid eutectic Si.

The dissolution of Mg_2Si and the diffusion of its Mg and Si atoms into the α-Al matrix are fundamental aspects of allowing precipitation hardening after the solution (T4) heat treatment. Figure 3 shows that the cast samples precipitated Mg_2Si in the grain boundaries, which may be diffused into the α-Al matrix. Figure 3 further proves the presence of Mg_2Si by the peak highlighted (Mg_2Si peak, 553 °C), while the eutectic Si and α-Al peaks were observed at 574 °C and 605 °C, respectively. The liquidus temperature for the A356 alloy with ultrasonically treated melt was observed to occur at 611 °C. The reported temperatures are well within the range of accepted temperatures for this alloy [24].

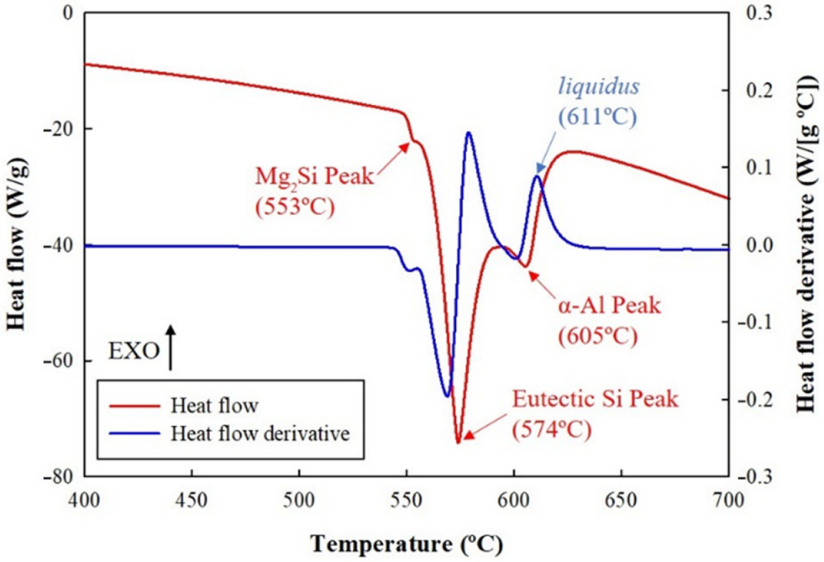

Figure 3. DTA analysis (heating) of as-cast sample detailing the melting of Mg_2Si, eutectic Si and α-Al.

Indeed, the dissolution of the Mg_2Si and the diffusion of the Si and Mg atoms are fundamental aspects of the solution treatment. After quenching, these solute atoms are able to assemble into vacancy-rich clusters (*VRCs*) [25] and follow the typical artificial aging precipitation sequence (Equation (1)) [26].

$$\alpha_{SS} \rightarrow VRC \rightarrow GP_{zones} \rightarrow \beta'' \rightarrow \beta' \rightarrow \beta(Mg_2Si) \quad (1)$$

Figure 4 and Table 3 detail the precipitate dissolution in the solution-treated (T4) and artificially aged samples (T6). *VRCs* were only detected in the solution-treated (T4) sample, meaning that there is a solution able to precipitate. The presence of precipitates in this sample suggests residual precipitation (β'' to β) entrapped in the matrix after quenching, as reported by Kim et al. [27]. Artificially aged (T6) samples display no significant presence of VRCs, meaning that the solution was diffused and precipitated.

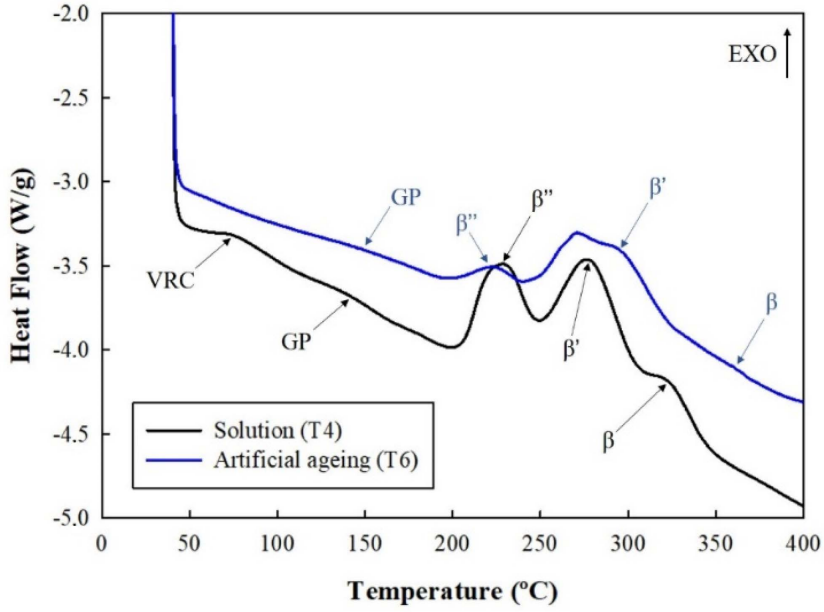

Figure 4. DSC analysis (heating) of solution-treated (T4) and artificially aged (T6) samples detailing the dissolution of the precipitates.

Table 3. Detail of precipitate dissolution temperature and energy in solution-treated (T4) and artificially aged (T6) samples.

Precipitate	Sample			
	Solution-Treated (T4)		Artificially Aged (T6)	
	Peak Temperature (°C)	Energy (J/g)	Peak Temperature (°C)	Energy (J/g)
VRC	77	0.6		
GP zones	140	0.4	148	0.2
β''	229	4.9	223	0.8
β'	278	6.5	294	10.9
β (Mg_2Si)	325	1.1	357	0.1

In addition to the *VRCs*, the dissolution energies in Table 3 attest that the solution-treated (T4) sample has a higher volume fraction of metastable *GP zones* with small radii β'' precipitates. The artificially aged (T6) samples reveal that the peak-aged state is composed of β'' and β' precipitates. Indeed, it is accepted that peak aging is formed by the higher volume fraction of precipitates with a size smaller than the critical radius, as precipitation strengthening (σ_{PPT}) in this condition is given by Equation (2) [28]. It is accepted that β'' and β' peak-aged samples are composed of a small volume fraction of coarse β'' and a high volume fraction of fine β' (i.e., $r < r_{crit}$), as supported by the dissolution energies presented in Table 3. The increase in the volume fraction (f_r) with radii in the vicinity of the critical value implies a significant increase in precipitation strengthening (σ_{PPT}).

$$\sigma_{PPT} = c_1 f_r^{\frac{1}{2}} < r >^{\frac{1}{2}} \quad \rightarrow \quad < r >< r_{crit} \tag{2}$$

Considering that the strengthening of an A356 alloy (σ_y, Equation (3)) [25] is composed of components of the pure aluminum strength (σ_i), solid solution strengthening (σ_{SS}) and precipitation strengthening (σ_{PPT}), the results from hardness testing (Figure 5) seem to corroborate the thermal analysis data, as shown by an increase in the precipitates fraction in Figure 4 and Table 3.

$$\sigma_y = \sigma_i + \sigma_{SS} + \sigma_{PPT} \tag{3}$$

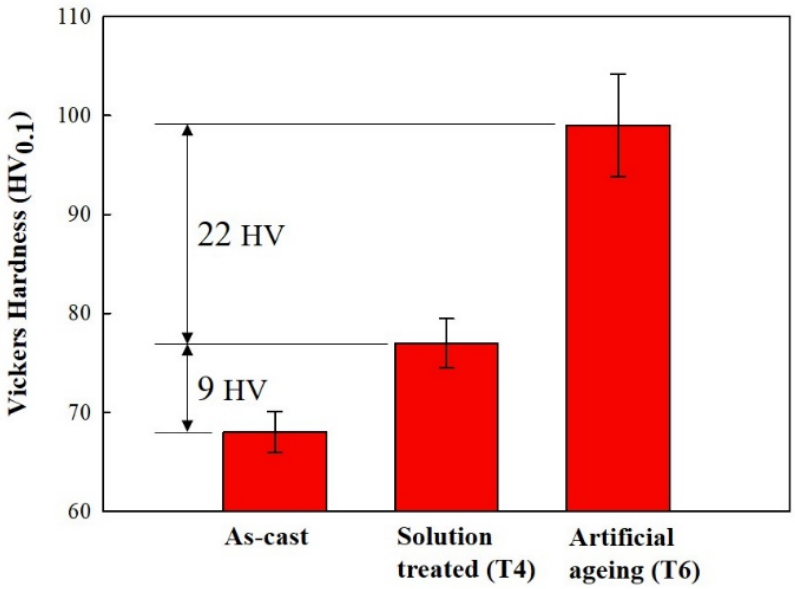

Figure 5. Microhardness of as-cast, solution-treated (T4) and artificially aged (T6) samples.

Considering that the initial pure aluminum strength (σ_i) is constant, the solution treatment that increases the solid solution strengthening (σ_{SS}) is dependent (Equation (4)) on the intrinsic solid solution strengthening (σ_{0SS}), the proportion of solution release (α) and volume fraction of the precipitates (f_r) [29]. It is proposed that there is an elevation in the intrinsic solution strengthening due to the dissolution of the Mg_2Si in the as-cast state (Figure 3) solution clustering into the *VRCs* that is shown in the solution-treated (T4) states in Figure 4 and Table 3. Given that there is a residual precipitation volume fraction (f_r) during the solution treatment (*GP zones* to β—Table 3) that is entrapped by quenching, there is an overall increase in 9 HVs, as presented in Figure 5. After the artificial aging (T6), mainly β' is entrapped by quenching (Table 3), resulting in an additional 22 Hv increase in hardness by the mechanisms discussed in Equation (2).

$$\sigma_{SS} = \sigma_{0SS}(1 - \alpha f_r)^{\frac{2}{3}} \quad (4)$$

Figure 6 displays the loss factor for the different tested samples under increasing strain amplitude, showing that both the solution treatment and the artificial aging induce significant changes in their damping response. The strain amplitude damping plots in Figure 6a show the typical behavior predicted by the Granato–Lücke theory [15,30], where there is a strain-independent damping (δ_0) behavior at lower values of strain amplitude, followed by a significant increase in internal friction in a strain-dependent damping domain (δ_H) [31].

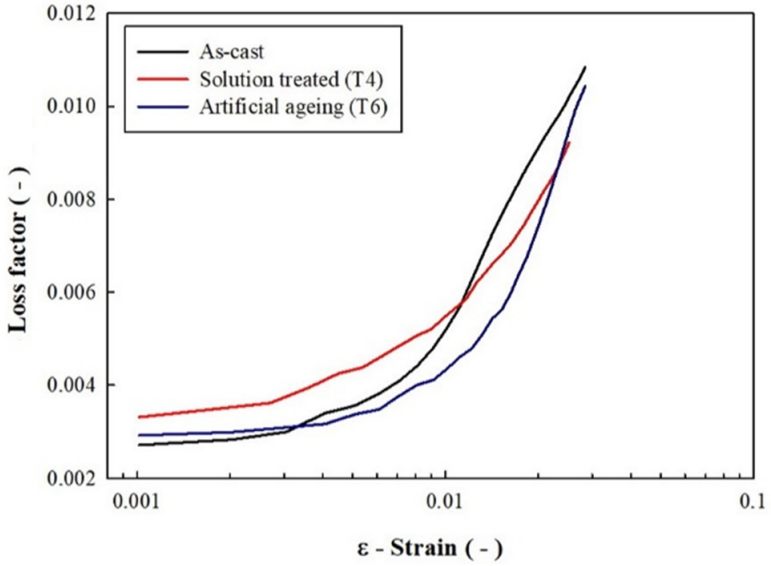

Figure 6. Damping capacity in as-cast, solution-treated (T4) and artificially aged (T6) states.

The strain-independent damping capacity (δ_0) is proportional to the dislocation density (ρ) and weak pinning point length (L_d), according to Equation (5) [32]. Considering the internal friction ($\delta = \pi\ tan(\delta)$) results, it is shown that the strain-independent damping capacity of the as-cast, solution-treated (T4) and artificial aging (T6) samples is 8.5×10^{-3}, 10.4×10^{-3} and 9.2×10^{-3}, respectively. The strain-dependent damping capacity reveals that there is an inversion in the damping capacity of the samples in this regime, in which the solution-treated (T4) samples display lower strain-independent damping than the artificially aged (T6) and as-cast samples.

Considering that at lower stress states (i.e., low strain amplitudes) there is no significant activation of mobile dislocations, the dislocation density (ρ) remains relatively constant and the changes in damping must be related to the changes in weak pinning length (L_d).

$$\delta_0 \sim \rho {L_d}^4 \quad (5)$$

Figure 7 shows the Granato–Lücke plots (Equation (6)) that were extracted from the strain-dependent damping capacity [29] for the samples in different states, supporting that the heat treatments are able to change the damping mechanisms in the matrix. This is particularly visible in the slopes and interceptions from which it is possible to extract the values of C_1 and C_2 (Table 4), respectively, in which the variables are directly related to the dislocation binding force (F_b), Bürger's vector (b), Young's modulus (E), dislocation density (ρ), weak pinning length (L_d) and strong pinning length (L_N) by Equations (7) and (8) [33].

$$\delta_H = \frac{C_1}{\varepsilon} e^{-\frac{C_2}{\varepsilon}} \tag{6}$$

$$C_1 = \frac{\rho F_b {L_N}^3}{6bEL_c} \tag{7}$$

$$C_2 = \frac{F_b}{bEL_c} \tag{8}$$

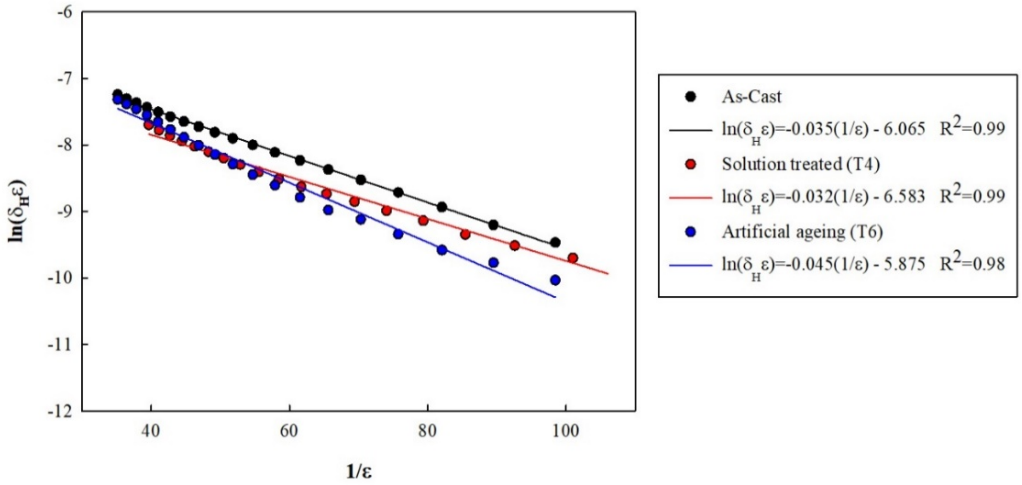

Figure 7. Granato–Lücke plots for as-cast, solution-treated (T4) and artificially aged (T6) samples.

Table 4. Detail of C_1 and C_2 variables extracted from the Granato–Lücke plots for as-cast, solution-treated (T4) and artificially aged (T6) samples.

Sample	C_1	C_2
As-cast	0.0023	0.035
Solution-treated (T4)	0.0014	0.032
Artificially aged (T6)	0.0028	0.045

Considering that an inverse proportionality characterizes C_1 and C_2 to the weak pinning length (L_d), it may be concluded that after the solution treatment (i.e., T4 state) there is an increase in weak pinning length (L_d). This is supported by the dissolution of the Mg_2Si secondary phase monitored in Figure 3 and the spheroidization of the eutectic Si, which reduces weak pinning in the boundary pinning. Such transformation is supported by Shoeck's theory (Equation (9)) [34,35], which predicts an elevation in damping ($Q^{-1} = tan(\delta)$) by the increase in the radii (a_i, see Eutectic Si in Table 2) of the eutectic Si that acts as inclusion in a matrix with a volume (V) and Poisson's ratio (ν), due to shear stress (p_{13}) in a given shear component ($\overline{p_{13}}$).

$$Q^{-1} = \frac{1}{{p_{13}}^2} \frac{8(1-\nu)}{3\pi(2-\nu)} \frac{1}{V} \sum {a_i}^3 \left(\overline{{p_{13}}^2}\right)_i \tag{9}$$

Precipitation strengthening due to artificial aging inherently reduces damping in low-stress levels. However, Figure 6 shows an inversion of this behavior at high strain amplitudes. This means that the samples in their T4 state display lower damping at high-stress levels. Considering that in this regime, the changes in damping capacity are regulated by their strain-dependent component (δ_H, Equation (6)) and, consequently, by the value of C_1 and C_2. The progressive precipitation and coarsening of metastable *VRC*, *GP zones* and β'' that are later quenched and entrapped as β' in the T6 state (as demonstrated in Figure 4 and Table 3), significantly reduce the weak (L_d) and strong (L_H) pinning length. Thus, the increase in C_1 and C_2 (Table 4) effectively increases the rate at which the strain-dependent component (δ_H) increases with the strain amplitude, as shown in the experimental results presented in Figure 6.

4. Conclusions

Dynamic mechanical analysis was used to study the influence of solution treatment (T4) and artificial aging (T6) on the damping capacity of cast A356 samples. Microstructural analysis has shown that the melt treatment successfully promoted moderate grain refinement, eutectic Si modification and degassing, allowing the damping capacity changes to focus on the spheroidization of the eutectic Si and precipitation strengthening. The experimental results have shown that:

(i) In the strain-independent regime (δ_0), solution-treated samples increased the damping capacity (10.4×10^{-3}), relative to artificially aged (9.2×10^{-3}) and as-cast (8.5×10^{-3}) samples. The spheroidization of the eutectic Si in the as-cast→T4 transition increased the pinning length and, thus, the damping capacity. However, the nucleation and growth of the precipitates (mainly β') in the T4→T6 transition decreased the weak pinning length and, consequently, the damping capacity.

(ii) The damping capacity in the strain-dependent regime (δ_H) revealed that the solution-treated (T4) samples tend to display lower damping capacity than the as-cast and artificially aged (T6) samples. The activation of bowing in strong pinning points is decreased in the as-cast→T4 transition and, consequently, the same occurs to the strain-independent damping capacity. However, the nucleation of precipitates increased the locations that allow bowing, acting as strong pinning points. Therefore, the T4→T6 transition increased the strain-dependent damping capacity.

(iii) Damping capacity was significantly influenced by heat treatments, however, contrary to common assumptions, peak-aged samples may eventually display higher damping capacity when subjected to elevated strain amplitudes. This is especially relevant for optimizing the design of mechanical components with enhanced vibration damping under high-stress states.

Author Contributions: Conceptualization, V.H.C. and H.P.; methodology, V.H.C. and H.P.; validation, V.H.C., I.D. and H.P.; formal analysis, V.H.C., I.D. and H.P.; investigation, V.H.C. and J.G.; resources, D.S., I.D. and H.P..; data curation, V.H.C. and I.D.; writing—original draft preparation, V.H.C., I.D. and H.P.; visualization, J.G. and I.D.; supervision, V.H.C. and H.P.; project administration, D.S.; funding acquisition, D.S., I.D. and H.P. All authors have read and agreed to the published version of the manuscript.

Funding: This research was funded by PTDC/EMEEME/30967/2017 and NORTE-0145-FEDER-030967, co-financed by the European Regional Development Fund (ERDF) through the Operational Programme for Competitiveness and Internationalization (COMPETE 2020), under Portugal 2020, and by the Fundação para a Ciência e a Tecnologia—FCT I.P. national funds. Additionally, this work was supported by the Portuguese FCT, under the reference project UIDB/04436/2020. This work also acknowledges the financial support of the Portuguese Science Foundation for Science and Technology (FCT) under the projects UIDB/EMS/00481/2020 (TEMA) and CENTRO-01-0145-FEDER-022083 (Centro2020, PORTUGAL 2020, European Regional Development Fund). This work was financially supported by project PRIDOP (POCI-01-0247-FEDER-040271), co-financed by the European Community Fund FEDER through POCI—Programa Operacional Competitividade e Internacionalização.

Data Availability Statement: The data presented in this study are available on request from the corresponding author. The data are not publicly available due to being part of an ongoing study.

Conflicts of Interest: The authors declare no conflict of interest.

References

1. Azimi, H.; Nourouzi, S.; Jamaati, R. Effects of Ti Particles and T6 Heat Treatment on the Microstructure and Mechanical Properties of A356 Alloy Fabricated by Compocasting. *Mater. Sci. Eng. A* **2021**, *818*, 141443. [CrossRef]
2. Carneiro, V.H.; Puga, H.; Meireles, J. Heat Treatment as a Route to Tailor the Yield-Damping Properties in A356 Alloys. *Mater. Sci. Eng. A* **2018**, *729*, 1–8. [CrossRef]
3. Erzi, E.; Gürsoy, Ö.; Yüksel, Ç.; Colak, M.; Dispinar, D. Determination of Acceptable Quality Limit for Casting of A356 Aluminium Alloy: Supplier's Quality Index (SQI). *Metals* **2019**, *9*, 957. [CrossRef]
4. Öztürk, İ.; Hapçı Ağaoğlu, G.; Erzi, E.; Dispinar, D.; Orhan, G. Effects of Strontium Addition on the Microstructure and Corrosion Behavior of A356 Aluminum Alloy. *J. Alloy. Compd.* **2018**, *763*, 384–391. [CrossRef]
5. Carneiro, V.H.; Rawson, S.D.; Puga, H.; Meireles, J.; Withers, P.J. Additive Manufacturing Assisted Investment Casting: A Low-Cost Method to Fabricate Periodic Metallic Cellular Lattices. *Addit. Manuf.* **2020**, *33*, 101085. [CrossRef]
6. Carneiro, V.H.; Rawson, S.D.; Puga, H.; Withers, P.J. Macro-, Meso- and Microstructural Characterization of Metallic Lattice Structures Manufactured by Additive Manufacturing Assisted Investment Casting. *Sci. Rep.* **2021**, *11*, 4974. [CrossRef]
7. Zhang, X.; Huang, L.K.; Zhang, B.; Chen, Y.Z.; Duan, S.Y.; Liu, G.; Yang, C.L.; Liu, F. Enhanced Strength and Ductility of A356 Alloy Due to Composite Effect of Near-Rapid Solidification and Thermo-Mechanical Treatment. *Mater. Sci. Eng. A* **2019**, *753*, 168–178. [CrossRef]
8. Zhang, Y.; Ma, N.; Le, Y.; Li, S.; Wang, H. Mechanical Properties and Damping Capacity after Grain Refinement in A356 Alloy. *Mater. Lett.* **2005**, *59*, 2174–2177. [CrossRef]
9. Zhang, Y.; Ma, N.; Wang, H.; Li, X. Study on Damping Behavior of A356 Alloy after Grain Refinement. *Mater. Des.* **2008**, *29*, 706–708. [CrossRef]
10. Mohd Noor, M.; Shamsul, J.; Kamarudin, H. Comparison of Dynamic Mechanical Properties of Non-Superheated and Superheated A357 Alloys. *S Kovove Mater.* **2017**, *48*, 6.
11. Rojas, J.I.; Venkata Siva, B.; Sahoo, K.L.; Crespo, D. Viscoelastic Behavior of a Novel Aluminum Metal Matrix Composite and Comparison with Pure Aluminum, Aluminum Alloys, and a Composite Made of Al–Mg–Si Alloy Reinforced with SiC Particles. *J. Alloy. Compd.* **2018**, *744*, 445–452. [CrossRef]
12. Carneiro, V.H.; Puga, H. Solution Treatment Enhances Both Static and Damping Properties of Al–Si–Mg Alloys. *Metall. Mater. Trans. A* **2018**, *49*, 5942–5945. [CrossRef]
13. Carneiro, V.H.; Puga, H. T6 Heat Treatment Impact on the Random Frequency Vibration Stress of Al–Si–Mg Alloys. *Met. Mater. Int.* **2019**, *25*, 880–887. [CrossRef]
14. Fu, S.; Li, S.; Luo, N.; Elena, M. Dynamic Optimization of Tracked Vehicle Power Train Based on Torsional Vibration Analysis. *Adv. Mech. Eng.* **2016**, *8*, 1687814016647304. [CrossRef]
15. Granato, A.; Lücke, K. Theory of Mechanical Damping Due to Dislocations. *J. Appl. Phys.* **1956**, *27*, 583–593. [CrossRef]
16. Vandersluis, E.; Ravindran, C. Comparison of Measurement Methods for Secondary Dendrite Arm Spacing. *Metallogr. Microstruct. Anal.* **2017**, *6*, 89–94. [CrossRef]
17. Puga, H.; Barbosa, J.; Azevedo, T.; Ribeiro, S.; Alves, J.L. Low Pressure Sand Casting of Ultrasonically Degassed AlSi7Mg0.3 Alloy: Modelling and Experimental Validation of Mould Filling. *Mater. Des.* **2016**, *94*, 384–391. [CrossRef]
18. Puga, H.; Barbosa, J.; Carneiro, V.H. The Role of Acoustic Pressure during Solidification of $AlSi_7Mg$ Alloy in Sand Mold Casting. *Metals* **2019**, *9*, 490. [CrossRef]
19. Eskin, D.G.; Tzanakis, I.; Wang, F.; Lebon, G.S.B.; Subroto, T.; Pericleous, K.; Mi, J. Fundamental Studies of Ultrasonic Melt Processing. *Ultrason. Sonochem.* **2019**, *52*, 455–467. [CrossRef]
20. Puga, H.; Barbosa, J.; Carneiro, V.H.; Barbosa, F.V.; Teixeira, J.C. Optimizing High-Volume Ultrasonic Melt Degassing Using Synchronized Kinematic Translation. *J. Mater. Res. Technol.* **2021**, *14*, 2832–2844. [CrossRef]
21. Yang, C.; Li, Y.; Dang, B.; Lü, H.; Liu, F. Effects of Cooling Rate on Solution Heat Treatment of As-Cast A356 Alloy. *Trans. Nonferrous Met. Soc. China* **2015**, *25*, 3189–3196. [CrossRef]
22. Ogris, E.; Wahlen, A.; Lüchinger, H.; Uggowitzer, P.J. On the Silicon Spheroidization in Al–Si Alloys. *J. Light Met.* **2002**, *2*, 263–269. [CrossRef]
23. Birol, Y. Impact of Grain Size on Mechanical Properties of AlSi7Mg0.3 Alloy. *Mater. Sci. Eng. A* **2013**, *559*, 394–400. [CrossRef]
24. Backerud, L.; Chai, G.; Tamminen, J. Solidification Characteristics of Aluminum Alloys. Vol. 2. Foundry Alloys. *Am. Foundrymen's Soc. Inc.* **1990**, *1990*, 266.
25. Liu, M.; Guo, Q.; Zhang, X.; Wüstenhagen, M.; Čížek, J.; Banhart, J. Clustering Phenomena in Quenched Al, Al–Mg, Al–Si and Al–Mg–Si Alloys. *Scr. Mater.* **2020**, *177*, 203–207. [CrossRef]
26. Edwards, G.A.; Stiller, K.; Dunlop, G.L.; Couper, M.J. The Precipitation Sequence in Al–Mg–Si Alloys. *Acta Mater.* **1998**, *46*, 3893–3904. [CrossRef]

27. Kim, S.; Song, M.; Lee, J.; Kim, J. The Nanocluster Formation and Vacancy Behavior of Step-Quenched Al–Mg–Si Alloy and Its Effect on Transition to β″ Phase via Advanced Methods. *Mater. Sci. Eng. A* **2021**, *811*, 141032. [CrossRef]
28. Colley, L.J.; Wells, M.A.; Poole, W.J. Microstructure–Yield Strength Models for Heat Treatment of Al–Si–Mg Casting Alloys II: Modelling Microstructure and Yield Strength Evolution. *Can. Metall. Q.* **2014**, *53*, 138–150. [CrossRef]
29. Puga, H.; Carneiro, V.H. Light-Alloy Melt Ultrasonication: Shorter T6 with Higher Precipitation Strengthening. *Met. Mater. Int.* **2021**, *27*, 3195–3204. [CrossRef]
30. Lücke, K.; Granato, A.V. Simplified Theory of Dislocation Damping Including Point-Defect Drag. I. Theory of Drag by Equidistant Point Defects. *Phys. Rev. B* **1981**, *24*, 6991–7006. [CrossRef]
31. Jun, J.-H. Damping Behavior of Mg–Zn–Al Casting Alloys. *Mater. Sci. Eng. A* **2016**, *665*, 86–89. [CrossRef]
32. Puga, H.; Carneiro, V.H.; Barbosa, J.; Soares, D. Effect of Grain and Secondary Phase Morphologies in the Mechanical and Damping Behavior of Al7075 Alloys. *Met. Mater. Int.* **2016**, *22*, 863–871. [CrossRef]
33. Tang, Y.T.; Zhang, C.; Ren, L.B.; Yang, W.; Yin, D.D.; Huang, G.H.; Zhou, H.; Zhang, Y.B. Effects of Y Content and Temperature on the Damping Capacity of Extruded Mg-Y Sheets. *J. Magnes. Alloy.* **2019**, *7*, 522–528. [CrossRef]
34. Schoeck, G. Internal Friction Due to Precipitation. *Phys. Status Solidi B* **1969**, *32*, 651–658. [CrossRef]
35. Schoeck, G.; Bisogni, E. Internal Friction in Al-Ag Alloys. *Phys. Status Solidi B* **1969**, *32*, 31–40. [CrossRef]